https://doi.org/10.5194/egusphere-2026-4109
Preprint. Discussion started: 4 August 2026

Warm-Sector Heavy Rainfall over the Eastern China Plains: Identification, Characteristics, and Precursor Dynamic Signals

Weilong Deng [a, b], Jianping Guo [b, e*], Ning Li [b, c], Zhen Zhang [b, d], Yifei Wang [b], Yi Yang [a, *]

[a] *College of Atmospheric Sciences, Lanzhou University, Lanzhou 730000, China*

[b] *State Key Laboratory of Severe Weather Meteorological Science and Technology & Specialized Meteorological Support Technology Research Center, Chinese Academy of Meteorological Sciences, China Meteorological Administration, Beijing 100081, China*

[c] *College of Earth and Planetary Sciences, University of Chinese Academy of Sciences, Beijing 100049, China*

[d] *Department of Atmospheric and Oceanic Sciences & Institute of Atmospheric Sciences, Fudan University, Shanghai 200438, China*

[e] *CMA Field Scientific Experiment Base for Low-Altitude Economy Meteorological Support of Unmanned Aviation in Guangdong-Hong Kong-Macao Greater Bay Area, Shenzhen 518108, China*

Correspondence to:

Dr./Prof. Jianping Guo (Email: jpguocams@gmail.com) and Dr./Prof. Yi Yang (Email: yangyi@lzu.edu.cn)

https://doi.org/10.5194/egusphere-2026-4109
Preprint. Discussion started: 4 August 2026

Abstract

Warm-sector heavy rainfall (WSHR) features small spatial scales, posing critical forecast challenges, while its fractional contribution to regional heavy rainfall and its short-term precursors remain poorly quantified. Drawing on 2021–2025 warm-season (June–September) observations from 493 surface rain gauges, ERA5 reanalysis, and a radar wind profiler (RWP) mesonet across the eastern China plains, we build an objective identification framework integrating automated front detection, warm-sector mask, and station-specific 99th-percentile hourly rainfall thresholds to separate WSHR from other heavy rain events. We detect 477 station-based WSHR events alongside 6002 non-warm-sector heavy rainfall events. WSHR exhibits scattered spatial distribution, peaks in July–August, and preferentially occurs overnight, with rainfall onset concentrated 2000–0300 Beijing Time. Accounting for merely 5–10% of annual heavy rainfall occurrences, WSHR has shorter durations yet comparable median rainfall accumulations and heavier extreme rainfall tails. On average, they contributed 13.8% of the total heavy-rainfall accumulation, and locally 40–50%. Composite ERA5 fields show that WSHR initiates within an 850-hPa moist tongue of high pseudo-equivalent potential temperature south of the front, superimposed on strengthening low-level moisture flux convergence. RWP composites based on 62 WSHR events reveal a characteristically low and strong low-level jet that becomes increasingly frequent before the onset of rainfall, accompanied by enhanced kinetic energy and shallow vertical shear below 3 km and an abrupt ascent increase centered at 1–2 km within the final hour. These kinematic signals from wind profilers offer valuable observational precursors for predicting localized WSHR across the eastern China plains.

https://doi.org/10.5194/egusphere-2026-4109
Preprint. Discussion started: 4 August 2026

1. Introduction

Warm-sector heavy rainfall (WSHR) occurs in the warm, moist air mass well ahead of a surface front, under weak synoptic-scale forcing (Huang et al., 1986; Sun et al., 2019; Wu et al., 2020). Because organized frontal lifting is absent, WSHR tends to be highly localized, to develop abruptly, to move slowly, and to concentrate intense rainfall over a confined area, producing disproportionate hazards through urban waterlogging, flash floods, and downstream river flooding (Zhang and Meng, 2019; Fu et al., 2023). As such, it is notoriously difficult to predict: operational global and regional models retain low quantitative precipitation forecast skill for WSHR events (Luo et al., 2017; Huang et al., 2025). Under weak synoptic-scale forcing, convective initiation is instead governed by mesoscale and boundary-layer processes, such as local convergence lines and boundary-layer jets, which operational models and conventional observations resolve only poorly (Wilson and Schreiber, 1986; Du and Chen, 2019). The regime therefore combines high societal impact with poor predictability.

Originally identified in South China during the pre-summer rainy season (Huang et al., 1986), WSHR has since been documented in several other regions of the country, including North China (Fu J. et al., 2020), the Yangtze–Huaihe coastal area (Yu et al., 2024), and the Sichuan Basin (Sun et al., 2019). The eastern China plains, which comprise the North China Plain and the middle-and-lower Yangtze Plain, are no exception. The region has experienced a number of WSHR events, including warm-shear-related events along the Yangtze–Huaihe coast during 2010–2017 (Yu et al., 2024), the localized rainstorm in Shijiazhuang on July 21, 2017 (He et al., 2021), and the extreme rainstorm over Beijing in late July 2025 (Wang et al., 2026). Mechanistic understanding has been built mainly from South China, where the low-level jet (LLJ), back-building mesoscale convective systems, and frontal–WS interactions have been identified as central controls on convection initiation and rainfall intensity (Wu and Luo, 2016; Du and Chen, 2018, 2019; Yang et al., 2024; Chen et al., 2025). In particular, double low-level jet structures have been shown to shape the regime there: the synoptic-system jet transports moisture, while the boundary-layer jet generates coastal

https://doi.org/10.5194/egusphere-2026-4109
Preprint. Discussion started: 4 August 2026

convergence and triggers convection near its terminus (Du and Chen, 2018, 2019). The nocturnal acceleration of the boundary-layer jet through the inertial oscillation (Blackadar, 1957) further explains the nighttime preference of warm-sector rainfall in that region. Over the eastern China plains, a smaller but growing body of work has begun to characterize WSHR through object-oriented composite analyses (Fu J. et al., 2020), localized case studies of warm-sector rainstorms on the plains (He et al., 2021), and reanalysis-based precursor diagnostics (Zhang et al., 2022).

Building on these advances, three directions deserve further investigation over the eastern China plains. The first is geographic. The mechanistic picture summarized above rests largely on South China, where coastline geometry, sea-breeze fronts, and warm marine moisture set the stage for the LLJ-driven coastal initiation that dominates the regime there. The eastern China plains operate under a different monsoonal and frontal climatology and lack much of that coastal forcing, so the controls established for the coast provide a strong starting point but need not transfer directly. Extending the analysis to this region therefore complements, rather than supplants, the South China work. The second concerns identification. Objective warm-sector criteria have been proposed for various regions of China (Wu et al., 2020; Li et al., 2021). Applying a consistent multi-year objective scheme of this kind to the eastern China plains would allow WSHR to be cleanly separated from other heavy rainfall, and its contribution to the regional total to be quantified on a directly comparable basis. The third concerns the pre-storm environment. Existing studies have established the broad synoptic and thermodynamic conditions that favor WSHR over the eastern China plains (e.g., Zhang et al., 2022; Yu et al., 2024). However, the limited time resolution of reanalyses and the sparse sampling of operational radiosondes have led that work to focus on conditions at the time of, rather than in the minutes-to-hours leading up to, convective initiation. Radar wind profilers (RWPs) sample the low-level wind continuously at high vertical and temporal resolution and are well suited to extend this picture into the pre-convective window. Profiler records have already yielded regional or nationwide LLJ climatologies (Du et al., 2012; Miao et al., 2018; Li et al., 2026), vertical divergence profiles of

https://doi.org/10.5194/egusphere-2026-4109
Preprint. Discussion started: 4 August 2026

demonstrated value for nowcasting convective storms (Guo et al., 2023), and evidence that the LLJ modulates the onset of summertime nocturnal rainfall in Beijing (Li et al., 2024). Moreover, the regional RWP network over the eastern China plains has accumulated sufficient data to support such an analysis.

Building on these foundations, this study brings together five warm seasons (2021–2025) of minute-resolution nationwide rain-gauge records, ERA5 reanalysis, and a RWP mesonet over the eastern China plains to pursue three objectives. First, we develop an objective scheme that separates warm-sector from other rainfall and identifies heavy rainfall events of both types, on the basis of automated front detection, a warm-sector mask, and a station-specific hourly intensity threshold. Second, we characterize the spatiotemporal distribution of WSHR, compare its event-scale properties with those of other heavy rainfall, and quantify its contribution to the total heavy-rainfall accumulation. Third, by leveraging minute-scale rain gauge records to pinpoint the onset of rainfall and high-frequency RWP measurements to track the pre-convective environment, we quantify the precursor dynamic signals leading up to WSHR genesis. Together, these objectives yield a consistent five-year, station-based picture of WSHR over the eastern China plains, and a set of profiler-observable precursor signals for this poorly predicted rainfall type. The remainder of the paper is organized as follows. Section 2 describes the data and the identification and diagnostic methods. Section 3 presents the spatiotemporal characteristics and the precursor signals. Section 4 discusses methodological strengths and limitations together with the physical mechanisms. Section 5 summarizes the main conclusions.

2. Data and methodology

2.1. Study region and period

The present study focuses on the eastern China plains, where heavy rainfall frequently occurs during the warm season (June–September) and poses substantial risks to densely populated and economically developed regions. The study period covers the warm seasons of 2021–2025. This period corresponds to the primary season of heavy

https://doi.org/10.5194/egusphere-2026-4109
Preprint. Discussion started: 4 August 2026

rainfall over eastern China, during which abundant moisture supply, active synoptic disturbances, and favorable mesoscale forcing frequently contribute to intense hourly rainfall.

Wang et al. (2023) documented a pronounced west-to-east intensification of extreme hourly precipitation across China, with the 95th-percentile hourly intensity attaining its annual high-value centers over the eastern China plains, including the North China Plain. Building on that result, here we examine the warm-season distribution and find that the high-value centers of the 99th-percentile hourly intensity ($R_{P_{99}}$) are likewise concentrated over the low-lying plains of eastern China. Figure 1a shows the spatial distribution of $R_{P_{99}}$ at 1708 national meteorological stations across central and eastern China during the warm seasons of 2021–2025, of which the rain gauges within our study region form a subset. The largest values are confined to the low-lying plains, indicating that these areas carry a high potential for intense hourly rainfall during the warm season. To focus on WSHR over relatively homogeneous low-terrain areas and to reduce the influence of complex terrain, the study region is defined as the portion of the eastern China plains bounded by 111.5–123.5°E and 30.5–40.7°N with terrain elevation at or below 200 m above sea level (dark blue contour in Fig. 1b).

Within this region, rain-gauge observations were used to identify rainfall events and to classify them into warm-sector rainfall and other rainfall categories. In addition, RWP observations at stations co-located with rain gauges were used to investigate the precursor dynamic signals associated with warm-sector rainfall events. As shown in Fig. 1b, the rain-gauge stations provide dense spatial coverage over the study region, while the co-located RWP and rain-gauge stations allow the pre-onset evolution of wind profiles to be directly linked to rainfall initiation.

2.2. Rain gauge and RWP measurements

Rain gauge and RWP measurements were obtained from the National Meteorological Information Center of the China Meteorological Administration (CMA), and strict quality control was applied. Additional data-availability criteria were

https://doi.org/10.5194/egusphere-2026-4109
Preprint. Discussion started: 4 August 2026

further applied to ensure the reliability of the datasets.

The rain gauge observations have a temporal resolution of 1 min. To ensure data completeness, only stations with data availability of at least 95% during June–September of 2021–2025 were retained. A total of 493 rain gauges within the study region satisfied this criterion, and their spatial distribution is shown in Fig. 1b. The 1-min rain gauge measurements were accumulated into both hourly and 6-min rainfall totals. The hourly totals were used to compute the station-specific threshold ($R_{P_{99}}$) and to identify WSHR events. The 6-min totals were used to pinpoint the precise onset time of rainfall and, in conjunction with the RWP observations, to characterize the precursor dynamic signals.

The RWP observations have a temporal resolution of 6 min and a vertical resolution of 120 m. A total of 79 stations with co-located RWP and rain gauge measurements were available within the study region, as shown in Fig. 1b. The quality-control procedure followed the methods of Wei et al. (2014) and Miao et al. (2018). Observations between 0.3 and 5 km above ground level (AGL) were used, corresponding to 39 vertical levels for each profile. Each wind profile was discarded if more than 40% of the data within the 0.3–5 km AGL height range were missing. Missing values in the remaining profiles were then estimated using linear interpolation. The RWP provides the full horizontal and vertical wind, all retained for the analyses that follow; only the ascent diagnostics (Fig. 12) are restricted to ascending velocities ($-w > 0$). These are therefore largely insensitive to hydrometeor fall-speed contamination, which appears as descent and is excluded, especially as the composites precede onset and are essentially free of precipitation. Residual biological or low-signal contamination was removed by the quality control above.

2.3. Identification of WSHR events

The identification of WSHR events draws on both ERA5 gridded fields and rain gauge observations. The ERA5 data used in this study cover 97–132°E and 22–57°N at a horizontal resolution of 0.25° and a temporal resolution of 1 h over the warm seasons

https://doi.org/10.5194/egusphere-2026-4109
Preprint. Discussion started: 4 August 2026

of 2021–2025; this domain is deliberately larger than the study region so that fronts in the vicinity of the gauges can be captured. The 1-min gauge measurements were accumulated to hourly totals to match the temporal resolution of ERA5, yielding a rainfall matrix $R(T_i, S_j)$ of dimension 14640 × 493, where T_i denotes the i-th hour (i = 1, 2, …, 14640) and S_j the j-th station (j = 1, 2, …, 493).

Synoptic fronts were identified objectively following an approach similar to that of Fu J. et al. (2020). The pseudo-equivalent potential temperature (θ_e) at 850 hPa was first computed from the ERA5 temperature and humidity fields (Bolton, 1980):

$$\theta_e = T_K \left(\frac{1000}{p}\right)^{0.2854(1-0.28\times10^{-3}r)} \times \exp\left[\left(\frac{3.376}{T_L} - 0.00254\right) r(1 + 0.81 \times 10^{-3} r)\right] \tag{1}$$

where T_K is the air temperature at 850 hPa (K), p is the pressure (hPa), r is the water-vapor mixing ratio (g kg^{-1}), converted from the ERA5 specific humidity, and T_L is the lifting condensation temperature (K), obtained following Bolton (1980) as

$$T_L = \frac{1}{\frac{1}{T_K - 55} - \frac{\ln(U/100)}{2840}} + 55 \tag{2}$$

where U is the relative humidity (%). The thermal front parameter (TFP) was then applied to detect fronts and to retrieve their synoptic attributes, including frontal type (cold, warm, or quasi-stationary), frontal length, and frontal position; these attributes are hereafter referred to as the synoptic front features, $SFF[T_i]$ (i = 1, 2, …, 14640) (see Sect. 1 in the Supplement for the full procedure).

In accordance with the criteria of Zhang et al. (2022) and Song et al. (2023), the warm sector is defined as the region where warm advection prevails at both 925 and 1000 hPa and the meridional wind component (v) is southerly (v > 0); the set of grid points satisfying this definition at hour T_i constitutes the warm-sector mask, $WSM[T_i]$.

The warm-sector rainfall criteria in our study follow the conceptual definition of earlier work, in which WSHR develops within the warm, moist air mass on the warm side of, and well separated from, a surface front under weak synoptic-scale forcing

https://doi.org/10.5194/egusphere-2026-4109
Preprint. Discussion started: 4 August 2026

(Huang et al., 1986; Chen et al., 2025). The 200–400 km distance band used below is likewise guided by previous studies: its lower bound keeps the samples clear of the frontal zone (Yang et al., 2024), and its upper bound confines them to the typical reach of the warm-sector ahead of the front (Chen et al., 2025). A rainy hour was classified as warm-sector rainfall only if the station simultaneously met both of the following:

(i) it lay on the southern side of the front, between 200 and 400 km from it; and

(ii) it fell within the warm-sector mask, $WSM[T_i]$.

Otherwise, it was classified as other rainfall. These two groups correspond to the warm- and cool-toned cells in Fig. 2, respectively, and each was further split by intensity into heavy ($R \geq R_{P_{99}}$; darker cells) and non-heavy ($0 < R < R_{P_{99}}$; lighter cells) rainfall, yielding the four labels. The rainfall label matrix $L(T_i, S_j)$, of the same dimension as $R(T_i, S_j)$, was initialized to N/A, and labels were assigned only to the station-hours with measurable rainfall ($R > 0$); all remaining entries were left as N/A. Accordingly, L is defined as

$$L(T_i, S_j) = \begin{cases} \mathrm{N/A}, & \text{no rainfall} \\ 1, & WSHR \\ 2, & \text{warm-sector non-heavy rainfall} \\ 3, & \text{other heavy rainfall} \\ 4, & \text{other non-heavy rainfall} \end{cases} \tag{3}$$

Considering the intermittency of rainfall, the labeled hourly records were grouped into events following Zhang et al. (2023), with successive events separated by a dry period of at least 3 h. An event that reached $R_{P_{99}}$ in at least one hour was treated as a heavy rainfall event, and was designated a WSHR event or other heavy rainfall event depending on whether all of the hours from the onset of rainfall to the first threshold-exceeding hour lay within the warm sector (a WSHR case is illustrated in Fig. 3d). An event never reaching $R_{P_{99}}$ was classified from the station location at onset, as a warm-sector non-heavy rainfall event or other non-heavy rainfall event according to whether the onset lay within the warm sector. Finally, any event influenced by a tropical cyclone (TC), defined as one with rainfall occurring within 500 km of a TC center according to the TC best-track dataset, was assigned to the other heavy or other non-heavy rainfall

https://doi.org/10.5194/egusphere-2026-4109
Preprint. Discussion started: 4 August 2026

event category (depending on its intensity), even if it would otherwise have satisfied the warm-sector rainfall criteria. This treatment keeps the WSHR sample free of TC-related circulations while leaving the event totals complete.

2.4. Event compositing and RWP-based precursor diagnostics

The precursor dynamic signals were investigated at the stations where an RWP and a rain gauge are co-located. To match the 6-min resolution of the RWP, each event's onset time was determined from the 6-min accumulated rainfall and rounded to the nearest 6-min mark (Li et al., 2024). The WSHR events occurring at these co-located stations were then used for the precursor analysis.

To characterize the environment in which WSHR develops, we additionally constructed station-relative composites of the ERA5 fields centered on each WSHR event. The target station of every event was shifted to the origin of a relative grid spanning ±3.5° in longitude and latitude. The 850-hPa specific humidity and θ_e, together with the low-level (1000–700 hPa) vertically integrated moisture flux divergence (VIMFD), were averaged over all WSHR events at 6 h and 3 h before onset and at the onset hour. Following the moisture-budget form of the water-vapor conservation equation (Banacos and Schultz, 2005) and the diagnostic procedure for reanalysis fields of Seager and Henderson (2013), VIMFD was obtained by first integrating the horizontal moisture flux over the 1000–700 hPa layer to form the vertically integrated moisture flux vector $Q = (Q_\lambda, Q_\varphi)$,

$$Q_\lambda = \frac{1}{g}\int_{p_t}^{p_s} qu\,dp, \qquad Q_\varphi = \frac{1}{g}\int_{p_t}^{p_s} qv\,dp \tag{4}$$

and then taking its horizontal divergence on the sphere,

$$VIMFD = \nabla \cdot Q = \frac{1}{a\,cos\varphi}\frac{\partial Q_\lambda}{\partial \lambda} + \frac{1}{a\,cos\varphi}\frac{\partial (Q_\varphi\,\cos\varphi)}{\partial \varphi} \tag{5}$$

where g is the gravitational acceleration, q the specific humidity, u and v the zonal and meridional wind components, p the pressure with p_s = 1000 hPa and p_t = 700 hPa the base and top of the integration layer, a the Earth's radius, and λ and φ the longitude and latitude. By convention, positive VIMFD denotes moisture flux

https://doi.org/10.5194/egusphere-2026-4109
Preprint. Discussion started: 4 August 2026

divergence and negative values denote convergence, so that the strengthening low-level moisture convergence preceding WSHR appears as increasingly negative VIMFD. These composites place the RWP-based kinematic diagnostics described below within their large-scale moisture and energy context.

For the WSHR events, the RWP signals were composited over the 180 min preceding the onset of rainfall. At each 6-min step and height level, we computed the mean wind profile, mean wind kinetic energy, mean vertical wind shear, the occurrence proportion and frequency of low-level jets (LLJs), the frequency of ascending motion, and the maximum ascent velocity. Tracking these signals through the pre-convective window characterizes how the low-level dynamic environment evolves as WSHR approaches onset.

Following the method proposed by Fu S. et al. (2020), the wind kinetic energy per unit mass is derived from the following equation:

$$KE = \frac{u^2 + v^2}{2} \tag{6}$$

where *u* and *v* are the zonal and meridional winds (m s^{-1}) and *KE* is in J kg^{-1}. Following previous convective-environment and wind-profiler studies (Markowski and Richardson, 2006; Thompson et al., 2007; Li et al., 2013; Zhang et al., 2020), the vertical wind shear (VWS) over a layer is taken as the magnitude of the bulk vector wind difference (top minus bottom) divided by the layer depth:

$$VWS = \frac{\sqrt{\left(u_{z_1} - u_{z_2}\right)^2 + \left(v_{z_1} - v_{z_2}\right)^2}}{z_1 - z_2} \times 1000 \tag{7}$$

where z_1 and z_2 are the top and bottom heights of the layer (m), u and v the corresponding winds (m s^{-1}), and the factor 1000 expresses VWS in 10^{-3} s^{-1}. The LLJ identification criteria are given in Sect. 2 in the Supplement.

3. Results

3.1. Spatiotemporal characteristics of WSHR

A total of 477 WSHR events were identified within the study region during the warm seasons of 2021–2025. Their spatial distribution is markedly sparse and scattered

https://doi.org/10.5194/egusphere-2026-4109
Preprint. Discussion started: 4 August 2026

(Fig. 4a): a large fraction of the 493 stations recorded no WSHR event at all (open circles), most of the remaining stations registered only one or two events, and merely a handful reached three to five. The higher counts show a weak preference for the southern and, in particular, the southeastern parts of the region, but they do not organize into a coherent spatial gradient, nor do they exhibit any systematic dependence on terrain. This lack of terrain dependence is unsurprising given the deliberately low and homogeneous relief (≤ 200 m) of the study region. This patchy, quasi-random spatial signature is consistent with the weakly forced, locally triggered character of warm-sector convection, in which the absence of strong synoptic lifting leaves convective initiation to be governed by mesoscale and boundary-layer processes.

Temporally, WSHR is concentrated in midsummer, with the great majority of events occurring in July and August and very few in June or September (Fig. 4b). Its diurnal distribution is bimodal: a weaker afternoon mode around 1300–1600 Beijing Time (BJT) is accompanied by a dominant nocturnal-to-postmidnight mode spanning roughly 2000–0300 BJT, the latter containing the highest event counts of the entire distribution.

For comparison, 6002 other heavy rainfall events were identified over the study period. Their spatial distribution is both ubiquitous and well organized (Fig. 5a). Every station in the study region recorded at least five events. Event counts increase from north to south, with the maxima concentrated in the south and especially the southeastern corner of the region, decreasing northward to 6–15. Diurnally, other heavy rainfall displays a strong, sharply defined late-afternoon maximum around 1400–1800 BJT, most pronounced in July and characteristic of thermally driven convection (Fig. 5b); a secondary nocturnal signal (about 2200–0200 BJT) also emerges in July, but the afternoon peak clearly dominates.

The two categories therefore differ not only in frequency but also in spatial organization and diurnal phase. Both share the dual (afternoon and nocturnal) diurnal character previously documented for the region between the Yellow and Yangtze rivers, where short-duration rainfall tends to peak in the late afternoon while longer-lived,

https://doi.org/10.5194/egusphere-2026-4109
Preprint. Discussion started: 4 August 2026

nocturnal episodes constitute a second maximum (Yu et al., 2007a, b; He and Zhang, 2010). However, their relative emphasis is reversed: other heavy rainfall is afternoon-dominated, pointing to surface heating and the associated growth of conditional instability, whereas WSHR is comparatively more nocturnal. This nocturnal preference, together with the scattered and weakly organized spatial pattern, points to a forcing distinct from daytime thermal convection. A natural candidate is the nocturnal acceleration of the low-level jet through the inertial oscillation, which after sunset strengthens the warm, moist southerly flow and the convergence and conditional instability at its terminus, and which has been widely linked to warm-sector and nocturnal rainfall (Du and Chen, 2018, 2019). In this respect the eastern China plains echo South China, where warm-sector rainfall peaks at night to early morning under nocturnal low-level-jet forcing, in contrast to the afternoon peak of frontal rainfall. These contrasts motivate the analysis of the precursor dynamic environment presented in the following sections, which examines how the low-level environment evolves in the hours preceding the onset of WSHR events.

3.2. Comparison between WSHR and other heavy rainfall events

Summed over all stations in the study region, WSHR events accounted for roughly 5–10% of all heavy rainfall events in each year of the study period (Fig. 6a). Against annual totals of 1131–1541 events, WSHR events numbered 72–125 per year, with the remaining 1019–1416 classified as other heavy rainfall. The two categories differ systematically in their event-scale characteristics, as detailed below.

The probability density function (PDF) of event duration (Fig. 6b) is shifted toward shorter durations for WSHR events: their median duration is 5.7 h, compared with 6.8 h for other heavy rainfall, and their 10^{th}–90^{th} percentile range is correspondingly narrower (2.1–13.4 h versus 2.5–17.6 h). The distribution of WSHR events also peaks higher and earlier, indicating a stronger concentration at short durations. The PDF of event cumulative rainfall (Fig. 6c) shows a complementary pattern. Although the median accumulations are comparable (70.3 mm for WSHR

https://doi.org/10.5194/egusphere-2026-4109
Preprint. Discussion started: 4 August 2026

versus 76.2 mm for other heavy rainfall), the distribution of WSHR events is broader and possesses a markedly heavier upper tail, with a 90th percentile of 156.1 mm against 120.2 mm for other heavy rainfall. The other-category PDF, by contrast, is more sharply peaked at moderate amounts. Because WSHR events attain these comparable or larger totals over systematically shorter durations, they imply higher mean rainfall rates and a greater propensity for rapid, extreme short-duration rainfall. This combination of brief duration and large accumulation is precisely the behavior that makes WSHR hazardous and difficult to anticipate, consistent with the localized, sudden, and poorly predictable nature of warm-sector convection reported in previous studies (Du and Chen, 2018; Fu J. et al., 2020).

The accumulated rainfall at each station from WSHR events (Fig. 6d) exhibits a clear spatial structure that echoes the pattern of event frequency in Fig. 4a. Accumulations increase toward the south and, most prominently, the southeastern corner of the region, where many stations exceed 300–500 mm, whereas the northern stations generally remain below about 150 mm. To gauge the importance of this contribution, we computed at each station the ratio of WSHR to total (WSHR plus other heavy rainfall) heavy rainfall accumulation (Fig. 6e). Across the study region this contribution rate averages 13.8% (median 12.4%), and the inset PDF is positively skewed, with its peak and median at low contribution rates but a long tail extending toward high values, where a substantial number of stations exceed 30% and local maxima reach 40–50%. Thus, although WSHR events are an order of magnitude less frequent than other heavy rainfall events, they account for an appreciable and locally dominant fraction of the total heavy rainfall accumulation over the eastern China plains, underscoring that they cannot be neglected in assessments of regional heavy rainfall and flood risk.

3.3. Pre-onset synoptic environment of WSHR

The station-relative composites introduced in Section 2.4 characterize the moisture and energy conditions in which WSHR develops. Averaged over all WSHR events, the

https://doi.org/10.5194/egusphere-2026-4109
Preprint. Discussion started: 4 August 2026

850-hPa specific humidity and θ_e fields display a consistent thermodynamic setting from 6 h before onset through the onset hour (Fig. 7), described below at the onset hour (Fig. 7c, f).

The composite specific humidity field at onset (Fig. 7c) places the event station within a moist tongue. Specific humidity at the station reaches 14.8 g kg^{-1}, close to the composite maximum; the moist core extends toward the southwest, and values decrease sharply to about 10 g kg^{-1} roughly 3° to the north. The station therefore lies near the northern, leading edge of the moist tongue, immediately upstream of the strong meridional moisture gradient that separates the warm, humid air from the drier air to the north. The composite θ_e field (Fig. 7f) reinforces this picture energetically. The station sits on the warm side of a pronounced θ_e gradient, where θ_e is about 350–352 K and decreases northward to roughly 336–340 K across a band of densely packed contours; this concentrated θ_e gradient marks the frontal zone, with the front lying to the north of the station. WSHR is therefore consistently found within the warm, humid, high-θ_e tongue on the warm (southern) flank of the front. Such an environment, rich in low-level moisture and high θ_e, supplies abundant water vapor and the conditional instability needed to sustain deep moist convection, in agreement with the warm, humid southerly boundary-layer flow long recognized as the moisture source and destabilizing agent for WSHR (Du and Chen, 2018).

The composite VIMFD field adds a dynamic dimension to this thermodynamic setting (Fig. 8). Low-level (1000–700 hPa) moisture flux convergence, shown by negative VIMFD, is present near the event station throughout the pre-onset window and intensifies as onset approaches. Six hours before the onset of rainfall, the convergence is modest and displaced to the west of the station (Fig. 8a), and it deepens by three hours before onset (Fig. 8b). At the onset of rainfall, a pronounced convergence core sits essentially on the station, with values below about -5×10^{-4} kg m^{-2} s^{-1} (Fig. 8c). This progressive concentration of low-level moisture convergence at the station, superimposed on the warm, humid, high-θ_e tongue, preconditions the column for the deep moist convection that produces WSHR and marks the transition from a merely

https://doi.org/10.5194/egusphere-2026-4109
Preprint. Discussion started: 4 August 2026

favorable thermodynamic background to active low-level forcing.

These composite conditions establish that WSHR develops in an environment that is favorable in terms of moisture, energy, and low-level moisture convergence. Such an environment, however, is a necessary but not a sufficient condition for convective initiation. Under the weak synoptic-scale forcing that characterizes the warm sector, mesoscale and boundary-layer dynamic processes are likely to play an important, and perhaps decisive, role in the triggering and intensification of convection. To identify these processes, the following section examines the precursor dynamic signals recorded by the radar wind profilers co-located with WSHR stations (Fig. 9a), focusing on how the low-level dynamic environment evolves in the hours preceding WSHR onset.

3.4. RWP-derived precursor dynamic signals for WSHR

Following the procedure described in Section 2.4, WSHR events were identified at the RWP stations that recorded WSHR. This screening yielded 62 WSHR events across 48 stations, on which the analysis of the precursor dynamic environment below is based. For each event, the RWP profiles were composited over the 180 min preceding onset (the same 3 h used in Section 2 to separate rainfall events), tracking the evolution of the low-level flow as onset approached.

In the mean wind profile (Fig. 9b), wind speed increases almost monotonically with height, from roughly 4 m s^{-1} near the surface to about 12 m s^{-1} at 5 km AGL, and the wind veers clockwise throughout the layer. This veering is a signature of low-level warm-air advection consistent with the warm, moist southerly flow and the high-θ_e tongue documented in Section 3.3. The composite rainfall in the 30 min after the onset of rainfall (green columns) rises sharply, confirming the high-intensity character of the WSHR events.

The wind kinetic energy shows a pronounced low-level signature (Fig. 9c). Although kinetic energy increases with height overall, the WSHR events exhibit a pronounced buildup of kinetic energy at low to middle levels (below about 3–4 km) in the hours leading up to onset. This low-level energization is a prominent feature of the

https://doi.org/10.5194/egusphere-2026-4109
Preprint. Discussion started: 4 August 2026

pre-onset window. It points to a progressive strengthening of the low-level flow before convective initiation.

The composite vertical wind shear (Fig. 10) is dominated by a shallow but intense layer of low-level shear. The strongest vertical wind shear (up to about 14×10^{-3} s^{-1}) is concentrated in bulk layers confined to the lowest 1.5 km or so (lower left of each panel), while deep-layer shear spanning the mid-troposphere is comparatively weak. This low-level vertical wind shear intensifies as the onset of rainfall approaches. Its prior-3-h composite mean is shown in Fig. 10a, while the time windows in Fig. 10b–f resolve the evolution. The vertical wind shear is relatively steady in the earlier windows (Fig. 10b, c), strengthens over the final hour (Fig. 10d, e), and, at the onset of rainfall, is joined by an additional band of strong vertical wind shear near 2–3 km (Fig. 10f). This deepening and intensification of the shear are consistent with the influence of a low, strong low-level jet that sharpens the vertical wind gradient across its core, an environment favorable for organizing and sustaining low-level convergence and convection.

Because the horizontal-wind precursor signals are concentrated below 3 km, the low-level wind was analyzed in greater detail (Fig. 11). The maximum wind speed below 3 km has a median of about 12 m s^{-1} that rises gradually toward onset, reaching its highest extreme values (upper whiskers up to about 25 m s^{-1}) in the final tens of minutes (Fig. 11a). Among the events containing an identifiable low-level jet (LLJ), the jet cores are generally low and strong (Fig. 11b): the mean core heights lie mostly below about 1.8 km AGL, and the mean core speeds range from roughly 11 to 26 m s^{-1}, above the 10 m s^{-1} identification threshold. Most notably, the LLJ occurrence frequency (Fig. 11c) increases from roughly 8–10% early in the window to about 20% within roughly the final 60 min before onset. This increase is statistically robust. Averaged over events, the LLJ occurrence in the final 60 min exceeds that in the first 60 min of the window by 7.0 percentage points, with a bootstrap 95% confidence interval of 0.1 to 14.1 percentage points (see Sect. 3 in the Supplement for the bootstrap procedure). Even at the onset of rainfall, only about 20% of the profiles contain an identifiable LLJ. The

https://doi.org/10.5194/egusphere-2026-4109
Preprint. Discussion started: 4 August 2026

sharp rise in LLJ occurrence, rather than the presence of the jet in most events, therefore marks the approach of the onset of rainfall. A low, strong LLJ, occurring with sharply rising frequency in the hour before the onset of rainfall, thus stands out as the most prominent dynamic signal preceding WSHR. This signal is consistent with the well-documented role of the boundary-layer low-level jet in transporting warm, moist air and generating low-level convergence ahead of its terminus (Du and Chen, 2018, 2019). For those events that occur at night, the nocturnal acceleration of the jet through the inertial oscillation may further reinforce this low-level forcing, a mechanism widely linked to warm-sector and nocturnal rainfall (Blackadar, 1957).

The strengthening low-level flow is accompanied by enhanced ascent. Throughout, only ascending velocities ($-w > 0$) are considered. Figure 12a shows, at each height and lead time, the frequency with which the events exhibit ascent (the fraction with $-w > 0$). This ascending-motion frequency increases as the onset of rainfall approaches. It is concentrated in the 1–3 km layer, with the highest frequencies, up to about 35%, centered near 1–2 km.

The per-event maximum ascent speed attained within each layer is summarized in Fig. 12b–e. Above 2 km the maximum ascent is comparatively weak: it is nearly steady at 3–5 km (Fig. 12b) and only modestly enhanced at 2–3 km (Fig. 12c). The strongest ascent is instead found in the low levels. In the 1–2 km layer (Fig. 12d), $-w$ increases sharply within the final 30 min or so before the onset of rainfall, with extreme values reaching about 1.0–1.4 m s^{-1}. These extremes are instantaneous per-event peak upward velocities rather than layer or composite means. Their magnitude is consistent with vigorous boundary-layer thermals and incipient convective updraft cores. Substantial ascent persists down into the 0.3–1 km layer (Fig. 12e), so that the strongest low-level upward motion is concentrated between about 0.3 and 2 km. The maximum ascent thus sits at 1–2 km, coincident with the level where the LLJ core and the strongest low-level convergence are found.

Taken together, these signals describe a coherent precursor chain for WSHR. In the final one to three hours before onset, the low-level jet becomes more frequent, with

https://doi.org/10.5194/egusphere-2026-4109
Preprint. Discussion started: 4 August 2026

characteristically low and strong cores, while low-level kinetic energy builds up and a shallow but strong low-level shear is maintained. The resulting low-level convergence forces an ascent that maximizes near 1–2 km and strengthens abruptly in the final 30 min or so. This ascent acts on the warm, humid, high-θ_e tongue and the strengthening moisture flux convergence identified in Section 3.3, triggering and intensifying the deep convection responsible for WSHR; latent-heat release then further deepens the moist updraft and sustains the rainfall. The pre-convective evolution is thus marked by a buildup of low-level kinetic energy, the emergence of a low and strong LLJ whose occurrence frequency rises sharply before the onset of rainfall, and an abrupt enhancement of ascent at 1–2 km. These precursor dynamic signals can all be observed in real time by an RWP, and together they characterize the pre-convective evolution of WSHR. As such, they may serve as candidate reference indicators for the imminent development of this poorly predicted class of heavy rainfall, although their event-level predictive skill requires further evaluation.

4. Discussion

4.1. Strengths and limitations of the identification and diagnostic framework

The objective scheme developed here separates WSHR from other heavy rainfall without manual synoptic typing, which is its main advance over the case-by-case or subjectively classified samples that dominate the warm-sector literature. Combining automated TFP detection (Hewson, 1998; Jenkner et al., 2010; Fu J. et al., 2020) with a warm-sector mask, a fixed 200–400 km distance band, and a locally defined 99th-percentile intensity threshold, the method yields a homogeneous five-year sample of 477 WSHR and 6002 other heavy rainfall events across 493 stations. This consistency makes the comparisons in Sections 3.1 and 3.2 reproducible and removes the subjectivity that complicates earlier intercomparisons.

Several limitations temper this strength. The front and warm-sector fields come from ERA5 at 0.25° and hourly resolution (Hersbach et al., 2020), which represents synoptic fronts well but smooths drylines, outflow boundaries, and other mesoscale

https://doi.org/10.5194/egusphere-2026-4109
Preprint. Discussion started: 4 August 2026

features, so a minority of events near them may be misattributed. TFP detection places the front within the baroclinic zone rather than at its warm leading edge (Hewson, 1998), and the distance band and percentile thresholds, though physically motivated, were not tuned by sensitivity tests. Defining heavy relative to each station's climatology accommodates the south-to-north moisture gradient but mixes stations of very different absolute intensity. These choices warrant sensitivity tests in future work.

The RWP diagnostics are a second contribution. Continuous 6-min wind profiling captures pre-convective low-level flow evolution that hourly reanalyses and soundings fail to resolve (Du et al., 2012; Guo et al., 2023), allowing us to characterize the pre-onset dynamic environment of WSHR within a well-constrained warm-sector thermodynamic regime. The approach is nonetheless constrained by the single-point nature of each profiler. Vertical motion is inferred indirectly rather than measured as a divergence field, which would require profiler mesonets (Guo et al., 2023); the 0.3–5 km range omits the surface layer and the mid to upper troposphere. Finally, compositing 62 events smooths the large case-to-case variability seen in Figs. 11 and 12, so the composite signals are best read as robust mean tendencies, not event-level certainties. In addition, the present analysis characterizes the pre-convective evolution of WSHR without a non-heavy or non-warm-sector baseline. The specificity of these signals to WSHR, rather than to warm-season rainfall in general, therefore remains to be tested against control groups in future work.

4.2. Physical interpretation and possible mechanisms

Section 3 outlines a coherent dynamic pathway from the warm-sector environment to heavy rainfall. The thermodynamic stage is set by the warm, humid, high-θ_e tongue on the warm side of the front (Fig. 7), which supplies the water vapor and conditional instability required for deep moist convection. Such a thermodynamic background is favorable but, under weak synoptic-scale forcing, is not by itself sufficient to initiate WSHR. The strengthening low-level moisture flux convergence (Fig. 8) and the low-level dynamic signals documented below indicate that mesoscale and boundary-layer

https://doi.org/10.5194/egusphere-2026-4109
Preprint. Discussion started: 4 August 2026

processes, rather than the thermodynamic environment alone, govern the transition to heavy rainfall.

Foremost among these dynamic signals is the low-level jet. In the WSHR events the low-level jet becomes markedly more frequent during the final hour before onset, with characteristically low and strong cores (Fig. 11), accompanied by a buildup of low-level kinetic energy (Fig. 9) and a sharp rise in ascent peaking at 1–2 km (Fig. 12). This is consistent with the established role of the boundary-layer jet in generating low-level convergence near its terminus and triggering convection (Wilson and Schreiber, 1986; Banacos and Schultz, 2005; Du and Chen, 2019). For events that occur at night, its acceleration through the inertial oscillation may reinforce this forcing, consistent with the nocturnal summer rainfall documented for the region (Yu et al., 2007a, b). The low, strong jet cores (Fig. 11b) place the strongest convergence and ascent in the 1–2 km layer, where the maximum ascent is observed.

The shallow but intense low-level shear (Fig. 10) acquires significance in this context. Low-level (0–3 km) vertical wind shear is a primary control on the organization and longevity of moist convection (Weisman and Klemp, 1982; Rotunno et al., 1988). The strengthening of this shear toward onset, together with the additional shear layer that emerges near 2–3 km at initiation, is the kinematic signature of a strong low-level jet. An environment that combines strengthening low-level shear with vigorous low-level ascent favors more organized, longer-lived, or repeatedly regenerated convection, which offers a dynamical route to the larger accumulations of WSHR.

This route reconciles the apparently paradoxical event statistics of Section 3.2, in which WSHR events are shorter-lived than other heavy rainfall yet reach comparable median and heavier extreme accumulations. Following the ingredients framework of Doswell et al. (1996), heavy rainfall reflects sustained high rainfall rates, the product of strong ascent acting on moist, nearly saturated air at high precipitation efficiency. The 1–2 km ascent surge documented here, operating on the high-θ_e tongue, is well suited to producing such high rates, and if the resulting convection is quasi-stationary or back-building in the manner of extreme-rain-producing mesoscale convective

https://doi.org/10.5194/egusphere-2026-4109
Preprint. Discussion started: 4 August 2026

systems elsewhere (Schumacher and Johnson, 2005), large totals can accumulate over a short interval. The present single-site analysis cannot resolve this organizational mode directly, so the inference remains a hypothesis to be tested with radar.

The central new result is therefore a set of observable kinematic precursors. These include the buildup of low-level kinetic energy, the appearance of a low and strong LLJ whose occurrence frequency surges in the final hour, and the abrupt enhancement of ascent at 1–2 km. Together, they characterize the pre-convective evolution of WSHR. These low-level dynamic signals are not available from moisture and instability fields alone, and they are consistent with recent profiler-network evidence that low-level jets strengthen within roughly 30–120 min before nocturnal rainfall (Li et al., 2024).

4.3. Implications and directions for future work

These findings bear directly on the long-standing difficulty of forecasting WSHR, for which the quantitative precipitation forecast skill of operational global and regional models remains low (Luo et al., 2017). Because the precursor dynamic signals identified here are observable in real time by operational radar wind profilers, they may serve as candidate short-range reference indicators for this rainfall type. Specifically, a rapid increase in LLJ occurrence, the presence of a low and strong jet core, and an abrupt rise in 1–2 km ascent during the preceding hour together point to an elevated likelihood of imminent WSHR. Assimilating high-resolution profiler winds, which has improved convection-permitting forecasts in related settings (Guo et al., 2023), is a natural way to translate these signals into operational skill.

The statistical, composite nature of the analysis also defines its principal avenue for extension. Composites establish the mean precursor structure but average over the diversity of individual events, and they cannot confirm the causal chain or the convective organization inferred above. Detailed case studies of individual WSHR events are the necessary next step, combining the RWP records with weather-radar reflectivity and dual-polarization fields to test whether back-building or training organization underlies the large accumulations (Schumacher and Johnson, 2005; Wu

https://doi.org/10.5194/egusphere-2026-4109
Preprint. Discussion started: 4 August 2026

and Luo, 2016). Convection-permitting simulations could then verify the jet–convergence–ascent pathway and isolate the contributions of the nocturnal inertial oscillation, cold pools, and terrain. Pairing profilers with ground-based microwave radiometers for thermodynamic profiling, and deploying profiler mesonets for direct horizontal-divergence retrieval (Guo et al., 2023), would remove two of the present observational limitations. Finally, applying the identification framework to other monsoon regions and seasons would test the generality of the precursor signals reported here.

5. Conclusions

Using five warm seasons (2021–2025) of minute-resolution rain-gauge records, ERA5 fields, and radar wind profiler (RWP) observations, we developed an objective scheme to separate warm-sector heavy rainfall (WSHR) from heavy rainfall not satisfying the warm-sector criteria over the eastern China plains. We characterized the two types and identified the pre-convective dynamic signals that precede WSHR.

WSHR is comparatively infrequent (477 station-based events, about 5–10% of the annual heavy-rainfall events, against 6002 other events) and weakly organized in space, scattered across the region without a clear terrain or latitudinal gradient, in contrast to the south-to-north decrease of other heavy rainfall. Its onset is preferentially nocturnal, with a 2000–0300 BJT maximum and a weaker afternoon mode, whereas other heavy rainfall peaks in the late afternoon. Although individual WSHR events are shorter-lived, they reach comparable median and heavier extreme accumulations, implying higher rainfall rates and a propensity for rapid, extreme rainfall, and they contribute a non-negligible mean of 13.8% (locally 40–50%) of the total heavy-rainfall accumulation.

Composite RWP observations indicate that, within the warm, humid, high-θ_e environment where WSHR develops, the pre-onset low-level flow undergoes a marked kinematic evolution. This includes enhanced kinetic energy below 3 km, an increasingly frequent low-level jet with low, strong cores, intensified shallow vertical shear, and a marked increase in ascending motion near 1–2 km during the final hour

https://doi.org/10.5194/egusphere-2026-4109
Preprint. Discussion started: 4 August 2026

before onset, superimposed on strengthening low-level moisture flux convergence. These precursor dynamic signals are consistent with a jet-related lifting pathway that helps convert a favorable warm-sector environment into localized heavy rainfall. They characterize the pre-convective evolution of WSHR and may serve as candidate reference indicators, with their event-level predictive skill to be evaluated in future work.

Data availability

The processed data derived from rain-gauge observations, wind profiler radar measurements, and ERA5 reanalysis used in this study can be acquired from Deng and Guo (2026). The ERA5 dataset can be acquired via Copernicus Climate Change Service (C3S) CDS (Hersbach et al., 2023). The TC best-track dataset can be downloaded freely from https://tcdata.typhoon.org.cn/en/index.html.

Author contribution

Weilong Deng: Conceptualization, Methodology, Visualization, Writing (original draft preparation), Writing (review and editing). **Jianping Guo**: Conceptualization, Data curation, Funding acquisition, Validation, Writing (review and editing). **Ning Li**: Investigation, Methodology, Validation, Writing (review and editing). **Yi Yang**: Investigation, Methodology, Validation, Writing (review and editing). **Zhen Zhang**: Investigation, Validation. **Yifei Wang**: Methodology, Validation, Writing (review and editing).

Competing interests

The contact author has declared that none of the authors has any competing interests.

https://doi.org/10.5194/egusphere-2026-4109
Preprint. Discussion started: 4 August 2026

Acknowledgements

This work was financially supported by Henan Provincial Major Industrial Key Technology Tackling Project under grant 261000320600, the National Natural Science Foundation of China under grant 42325501, the Innovation and Development Special Project of the China Meteorological Administration under grant CXFZ2026J107, and Chinese Academy of Meteorological Sciences under grant 2024Z003.

References

Banacos, P. C. and Schultz, D. M.: The use of moisture flux convergence in forecasting convective initiation: Historical and operational perspectives, Weather Forecast., 20, 351–366, https://doi.org/10.1175/WAF858.1, 2005.

Blackadar, A. K.: Boundary Layer Wind Maxima and Their Significance for the Growth of Nocturnal Inversions, Bull. Am. Meteorol. Soc., 38, 283–290, https://doi.org/10.1175/1520-0477-38.5.283, 1957.

Bolton, D.: The computation of equivalent potential temperature, Mon. Weather Rev., 108, 1046–1053, https://doi.org/10.1175/1520-0493(1980)108<1046:TCOEPT>2.0.CO;2, 1980.

Chen, G., Wen, L., Chen, X., Hua, S., Xu, F., and Zhang, S.: Contrasts in microphysical characteristics between the Meiyu warm-sector and frontal heavy rainfall in East China, Geophys. Res. Lett., 52, e2025GL117902, https://doi.org/10.1029/2025GL117902, 2025.

Deng, W. and Guo, J.: Data for Warm-Sector Heavy Rainfall over the Eastern China Plains: Identification, Characteristics, and Precursor Dynamic Signals, Zenodo [data set], https://doi.org/10.5281/zenodo.21257973, 2026.

Doswell, C. A., Brooks, H. E., and Maddox, R. A.: Flash flood forecasting: An ingredients-based methodology, Weather Forecast., 11, 560–581, https://doi.org/10.1175/1520-0434(1996)011<0560:FFFAIB>2.0.CO;2, 1996.

Du, Y. and Chen, G.: Heavy rainfall associated with double low-level jets over Southern China. Part I: Ensemble-based analysis, Mon. Weather Rev., 146, 3827–3844, https://doi.org/10.1175/MWR-D-18-0101.1, 2018.

Du, Y. and Chen, G.: Heavy rainfall associated with double low-level jets over Southern China. Part II: Convection initiation, Mon. Weather Rev., 147, 543–565, https://doi.org/10.1175/MWR-D-18-0102.1, 2019.

https://doi.org/10.5194/egusphere-2026-4109
Preprint. Discussion started: 4 August 2026

Du, Y., Zhang, Q., Ying, Y., and Yang, Y.: Characteristics of Low-level Jets in Shanghai during the 2008-2009 Warm Seasons as Inferred from Wind Profiler Radar Data, J. Meteorol. Soc. Jpn., 90, 891–903, https://doi.org/10.2151/jmsj.2012-603, 2012.

Fu, J., Zhang, F., and Hewson, T. D.: Object-Oriented Composite Analysis of Warm-Sector Rainfall in North China, Mon. Weather Rev., 148, 2719–2735, https://doi.org/10.1175/MWR-D-19-0038.1, 2020.

Fu, S., Jin, S., Shen, W., Li, D., Liu, B., and Sun, J.: A kinetic energy budget on the severe wind production that causes a serious state grid failure in Southern Xinjiang China, Atmos. Sci. Lett., 21, e977, https://doi.org/10.1002/asl.977, 2020.

Fu, Y., Sun, J., Fu, S., and Zhang, Y.: Comparison between warm-sector and frontal heavy rainfall events in South China and the objective classification of warm-sector heavy rainfall events, Meteorol. Atmos. Phys., 135, 11, https://doi.org/10.1007/s00703-022-00949-8, 2023.

Guo, X., Guo, J., Zhang, D.-L., and Yun, Y.: Vertical divergence profiles as detected by two wind-profiler mesonets over East China: Implications for nowcasting convective storms, Q. J. Roy. Meteorol. Soc., 149, 1629–1649, https://doi.org/10.1002/qj.4474, 2023.

He, H. and Zhang, F.: Diurnal variations of warm-season precipitation over Northern China, Mon. Weather Rev., 138, 1017–1025, https://doi.org/10.1175/2010MWR3356.1, 2010.

He, L., Long, L., Chen, B., Wang, Y., Geng, F., and Yan, X.: A case study on the triggering mechanisms of localized warm-sector rainstorm, Meteorol. Atmos. Phys., 133, 1707–1717, https://doi.org/10.1007/s00703-021-00836-8, 2021.

Hersbach, H., Bell, B., Berrisford, P., Hirahara, S., Horányi, A., Muñoz-Sabater, J., Nicolas, J., Peubey, C., Radu, R., Schepers, D., Simmons, A., Soci, C., Abdalla, S., Abellan, X., Balsamo, G., Bechtold, P., Biavati, G., Bidlot, J., Bonavita, M., De Chiara, G., Dahlgren, P., Dee, D., Diamantakis, M., Dragani, R., Flemming, J., Forbes, R., Fuentes, M., Geer, A., Haimberger, L., Healy, S., Hogan, R. J., Hólm, E., Janisková, M., Keeley, S., Laloyaux, P., Lopez, P., Lupu, C., Radnoti, G., de Rosnay, P., Rozum, I., Vamborg, F., Villaume, S., and Thépaut, J.-N.: The ERA5 global reanalysis, Q. J. Roy. Meteorol. Soc., 146, 1999–2049, https://doi.org/10.1002/qj.3803, 2020.

Hersbach, H., Bell, B., Berrisford, P., Biavati, G., Horányi, A., Muñoz Sabater, J., Nicolas, J., Peubey, C., Radu, R., Rozum, I., Schepers, D., Simmons, A., Soci, C., Dee, D., and Thépaut, J.-N.: ERA5 hourly data on pressure levels from 1940 to present, Copernicus Climate Change Service (C3S) Climate Data Store (CDS) [data set], https://doi.org/10.24381/cds.bd0915c6, 2023.

Hewson, T. D.: Objective fronts, Meteorol. Appl., 5, 37–65, https://doi.org/10.1017/S1350482798000553, 1998.

Huang, P., Wan, Q., Li, L., and Hu, S.: Numerical simulation and analysis of the modulation effect of sub-grid turbulent orographic form drag on warm-sector heavy rainfall in South China, Atmos. Res., 318, 107991, https://doi.org/10.1016/j.atmosres.2025.107991, 2025.

Huang, S. S., and Coauthors: Heavy Rainfall over Southern China in the Pre-Summer Rainy Season, Guangdong Science and Technology Press, 244 pp., 1986 (in Chinese).

Jenkner, J., Sprenger, M., Schwenk, I., Schwierz, C., Dierer, S., and Leuenberger, D.: Detection and climatology of fronts in a high-resolution model reanalysis over the Alps, Meteorol. Appl., 17, 1–18, https://doi.org/10.1002/met.142, 2010.

Li, N., Guo, J., Wu, M., Zhang, F., Guo, X., Sun, Y., Zhang, Z., Liang, H., and Chen, T.: Low-level jet and its effect on the onset of summertime nocturnal rainfall in Beijing, Geophys. Res. Lett., 51, e2024GL110840, https://doi.org/10.1029/2024GL110840, 2024.

Li, N., Guo, J., Guo, X., Chen, T., Zhang, Z., Tang, N., Wang, Y., Yang, H., Zheng, Y., and Zhou, Y.: On the nationwide variability of low-level jets prior to warm-season nocturnal rainfall in China revealed by radar wind profilers, Atmos. Chem. Phys., 26, 3339–3356, https://doi.org/10.5194/acp-26-3339-2026, 2026.

Li, W., Bi, X., Sheng, L., Luo, Y., and Sun, J.: Modulations of Synoptic Weather Patterns on Warm-Sector Heavy Rainfall in South China: Insights from High-Density Observations with Principal Component Analysis, Front. Earth Sci., 9, 678230, https://doi.org/10.3389/feart.2021.678230, 2021.

Li, X., Guo, X., and Fu, D.: TRMM-retrieved cloud structure and evolution of MCSs over the northern South China Sea and impacts of CAPE and vertical wind shear, Adv. Atmos. Sci., 30, 77–88, https://doi.org/10.1007/s00376-012-2055-2, 2013.

Luo, Y., Zhang, R., Wan, Q., Wang, B., Wong, W. K., Hu, Z., Jou, B. J.-D., Lin, Y., Johnson, R. H., Chang, C.-P., Zhu, Y., Zhang, X., Wang, H., Xia, R., Ma, J., Zhang, D.-L., Gao, M., Zhang, Y., Liu, X., Chen, Y., Huang, H., Bao, X., Ruan, Z., Cui, Z., Meng, Z., Sun, J., Wu, M., Wang, H., Peng, X., Qian, W., Zhao, K.,

https://doi.org/10.5194/egusphere-2026-4109
Preprint. Discussion started: 4 August 2026

and Xiao, Y.: The Southern China Monsoon Rainfall Experiment (SCMREX), Bull. Am. Meteorol. Soc., 98, 999–1013, https://doi.org/10.1175/BAMS-D-15-00235.1, 2017.

Markowski, P. and Richardson, Y.: On the Classification of Vertical Wind Shear as Directional Shear versus Speed Shear, Weather Forecast., 21, 242–247, https://doi.org/10.1175/WAF897.1, 2006.

Miao, Y., Guo, J., Liu, S., Wei, W., Zhang, G., Lin, Y., and Zhai, P.: The climatology of low-level jet in Beijing and Guangzhou, China, J. Geophys. Res.-Atmos., 123, 2816–2830, https://doi.org/10.1002/2017JD027321, 2018.

Rotunno, R., Klemp, J. B., and Weisman, M. L.: A theory for strong, long-lived squall lines, J. Atmos. Sci., 45, 463–485, https://doi.org/10.1175/1520-0469(1988)045<0463:ATFSLL>2.0.CO;2, 1988.

Schumacher, R. S. and Johnson, R. H.: Organization and environmental properties of extreme-rain-producing mesoscale convective systems, Mon. Weather Rev., 133, 961–976, https://doi.org/10.1175/MWR2899.1, 2005.

Seager, R. and Henderson, N.: Diagnostic computation of moisture budgets in the ERA-Interim reanalysis with reference to analysis of CMIP-archived atmospheric model data, J. Clim., 26, 7876–7901, https://doi.org/10.1175/JCLI-D-13-00018.1, 2013.

Song, L., Zhang, L., Ma, X., Dong, F., and Zhi, X.: Objective Identification and Analysis of Warm-Sector Rainstorm with Warm-Shear Pattern over Yangtze–Huaihe River Region, Chinese J. Atmos. Sci., 47, 1709–1722, https://doi.org/10.3878/j.issn.1006-9895.2207.21220, 2023 (in Chinese).

Sun, J., Zhang, Y., Liu, R., Fu, S., and Tian, F.: A review of research on warm-sector heavy rainfall in China, Adv. Atmos. Sci., 36, 1299–1307, https://doi.org/10.1007/s00376-019-9021-1, 2019.

Thompson, R. L., Mead, C. M., and Edwards, R.: Effective Storm-Relative Helicity and Bulk Shear in Supercell Thunderstorm Environments, Weather Forecast., 22, 102–115, https://doi.org/10.1175/WAF969.1, 2007.

Wang, X., Jiang, W., Wu, J., Hou, P., Dai, Z., Rao, P., Ling, Z., and Deng, Y.: Extreme hourly precipitation characteristics of Mainland China from 1980 to 2019, Int. J. Climatol., 43, 2989–3004, https://doi.org/10.1002/joc.8012, 2023.

Wang, Z., Gao, H., and Dong, Y.: Refined characteristics and large-scale anomalous circulations associated with the "25.7" extreme rainstorm in Beijing, Trans. Atmos. Sci., 49, 217–227, https://doi.org/10.13878/j.cnki.dqkxxb.20260107005, 2026 (in Chinese).

Wei, W., Zhang, H. S., and Ye, X. X.: Comparison of low-level jets along the north coast of China in summer, J. Geophys. Res.-Atmos., 119, 9692–9706, https://doi.org/10.1002/2014JD021476, 2014.

Weisman, M. L. and Klemp, J. B.: The Dependence of Numerically Simulated Convective Storms on Vertical Wind Shear and Buoyancy, Mon. Weather Rev., 110, 504–520, https://doi.org/10.1175/1520-0493(1982)110<0504:TDONSC>2.0.CO;2, 1982.

Wilson, J. W. and Schreiber, W. E.: Initiation of convective storms at radar-observed boundary-layer convergence lines, Mon. Weather Rev., 114, 2516–2536, https://doi.org/10.1175/1520-0493(1986)114<2516:IOCSAR>2.0.CO;2, 1986.

Wu, M. and Luo, Y.: Mesoscale observational analysis of lifting mechanism of a warm-sector convective system producing the maximal daily precipitation in China mainland during pre-summer rainy season of 2015, J. Meteorol. Res., 30, 719–736, https://doi.org/10.1007/s13351-016-6089-8, 2016.

Wu, N., Ding, X., Wen, Z., Chen, G., Meng, Z., Lin, L., and Min, J.: Contrasting frontal and warm-sector heavy rainfalls over South China during the early-summer rainy season, Atmos. Res., 235, 104693, https://doi.org/10.1016/j.atmosres.2019.104693, 2020.

Yang, H., Du, Y., Chen, Z., and Fang, J.: Could developing frontal rainfall influence warm-sector rainfall?, Geophys. Res. Lett., 51, e2024GL110430, https://doi.org/10.1029/2024GL110430, 2024.

Yu, R., Xu, Y., Zhou, T., and Li, J.: Relation between rainfall duration and diurnal variation in the warm season precipitation over central eastern China, Geophys. Res. Lett., 34, L13703, https://doi.org/10.1029/2007GL030315, 2007a.

Yu, R., Zhou, T., Xiong, A., Zhu, Y., and Li, J.: Diurnal variations of summer precipitation over contiguous China, Geophys. Res. Lett., 34, L01704, https://doi.org/10.1029/2006GL028129, 2007b.

Yu, Y., Zhang, L., Song, L., Li, W., Zhou, L., and Ouyang, L.: Multiscale Features and Triggering Mechanisms of the Warm-Sector Heavy Rainfall Accompanied by Warm Shear Along the Yangtze–Huaihe Coastal Regions, J. Hydrometeorol., 25, 465–478, https://doi.org/10.1175/JHM-D-23-0143.1, 2024.

Zhang, L., Ma, X., Zhu, S., Guo, Z., Zhi, X., and Chen, C.: Analyses and applications of the precursor signals of a kind of warm-sector heavy rainfall over the coast of Guangdong, China, Atmos. Res., 280, 106425, https://doi.org/10.1016/j.atmosres.2022.106425, 2022.

Zhang, M. and Meng, Z.: Warm-Sector Heavy Rainfall in Southern China and Its WRF

https://doi.org/10.5194/egusphere-2026-4109
Preprint. Discussion started: 4 August 2026

Simulation Evaluation: A Low-Level-Jet Perspective, Mon. Weather Rev., 147, 4461–4480, https://doi.org/10.1175/MWR-D-19-0110.1, 2019.

Zhang, Y., Guo, J., Yang, Y., Wang, Y., and Yim, S. H. L.: Vertical windshear modulates particulate matter pollutions: A perspective from radar wind profiler observations in Beijing, China, Remote Sens., 12, 546, https://doi.org/10.3390/rs12030546, 2020.

Zhang, Y., Liang, K., and Liu, C.: Time distribution pattern and spatial heterogeneity of hourly scale event-based extreme precipitation in China, J. Hydrol., 622, 129712, https://doi.org/10.1016/j.jhydrol.2023.129712, 2023.

https://doi.org/10.5194/egusphere-2026-4109
Preprint. Discussion started: 4 August 2026

Figures

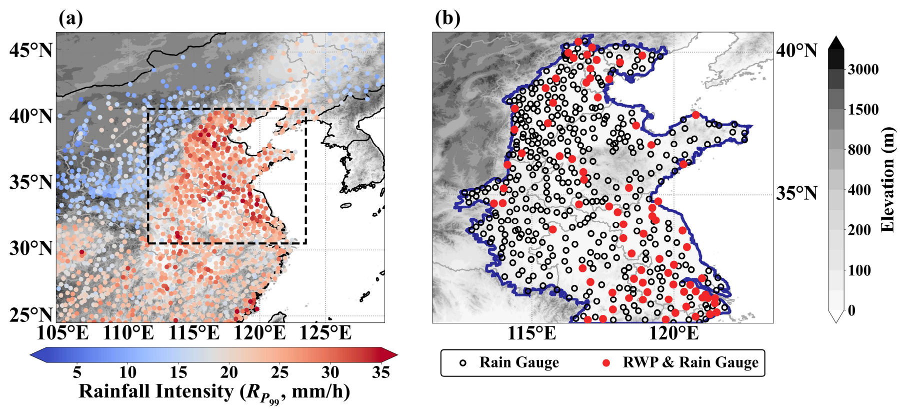

Figure 1. (a) Spatial distribution of 99th-percentile hourly rainfall intensity ($R_{P_{99}}$; mm h^{-1}) at rain gauges across eastern China during the warm seasons (June–September) of 2021–2025. Grayscale shading represents terrain elevation, and the dashed black rectangle marks the subdomain zoomed in panel (b). (b) Enlarged view of the study domain covering the eastern China plains. The dark blue contour denotes areas within 111.5–123.5°E and 30.5–40.7°N with terrain elevation at or below 200 m. Open black circles indicate standalone rain gauge sites, while red filled circles mark co-located radar wind profiler (RWP) and rain-gauge stations.

https://doi.org/10.5194/egusphere-2026-4109
Preprint. Discussion started: 4 August 2026

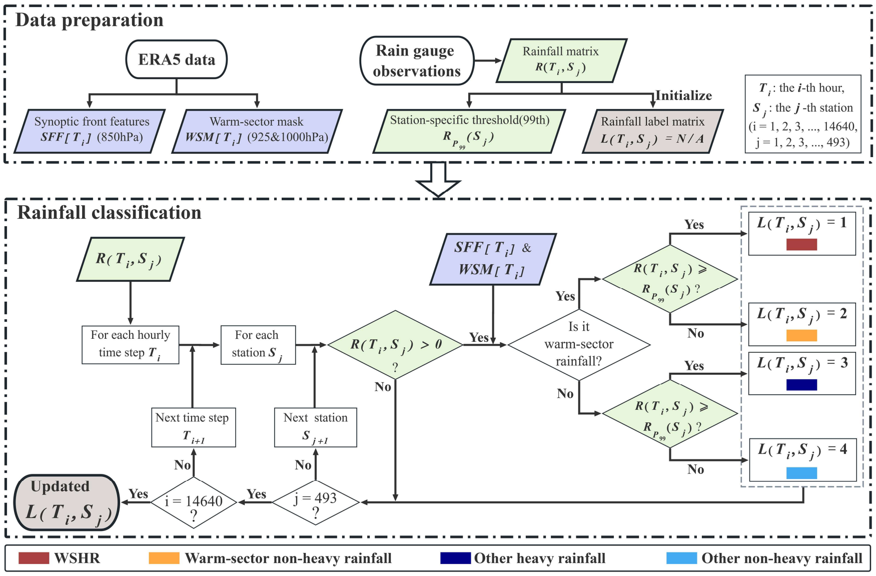

871

Figure 2. Flowchart illustrating the objective classification scheme for hourly rainfall observations at rain gauge stations. Four rainfall categories are defined: warm-sector heavy rainfall (WSHR, $L = 1$, dark red); warm-sector non-heavy rainfall ($L = 2$, orange); other heavy rainfall ($L = 3$, dark blue); and other non-heavy rainfall ($L = 4$, light blue).

https://doi.org/10.5194/egusphere-2026-4109
Preprint. Discussion started: 4 August 2026

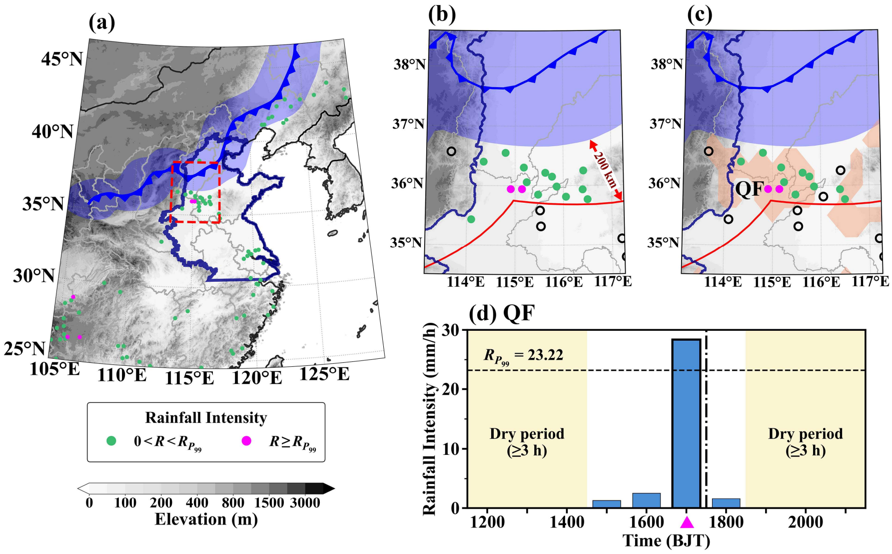

Figure 3. Example of an identified WSHR event at Qingfeng (QF) weather station on August 18, 2023. (a) Cold front (blue line) and its 200-km frontal zone (blue shading) at 1700 Beijing Time (BJT), with station rainfall overlaid (green dots: $0 < R < R_{P_{99}}$; magenta dots: $R \geq R_{P_{99}}$). (b) and (c) Enlarged views of the red dashed rectangle in (a): (b) shows rainfall at stations 200–400 km from the front (the warm-sector candidate region); (c) additionally shows the warm-sector mask (orange shading) and rainfall at stations falling within it. Open black circles denote stations with rainfall ($R > 0$) that fall outside the study region or fail the warm-sector criteria. (d) Hourly rainfall time series at QF station. The dashed line marks $R_{P_{99}}$ = 23.22 mm h⁻¹; the dash-dotted line marks the first hour reaching $R_{P_{99}}$, with all rainfall hours from onset to this hour required to lie within the warm sector. Yellow shading denotes dry periods (≥ 3 h) bounding the event, and the magenta triangle marks the hour identified as WSHR.

https://doi.org/10.5194/egusphere-2026-4109
Preprint. Discussion started: 4 August 2026

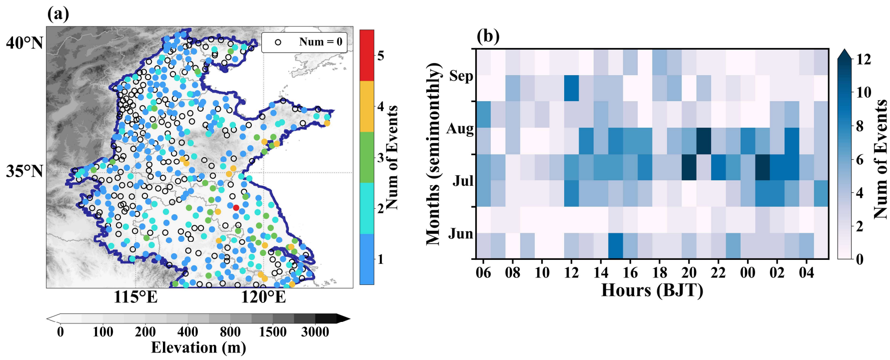

889

890 **Figure 4.** Spatiotemporal distribution of WSHR events over the eastern China plains
891 during the warm seasons (June–September) of 2021–2025. (a) Station-wise counts of
892 WSHR events; open black circles mark stations with zero detected events (Num = 0).
893 Grayscale shading denotes terrain elevation. (b) WSHR event counts by semimonthly
894 period and the hour of the onset of rainfall.

https://doi.org/10.5194/egusphere-2026-4109
Preprint. Discussion started: 4 August 2026

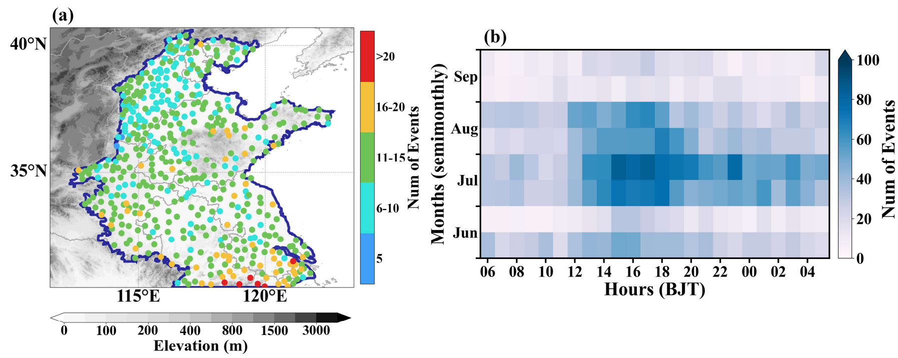

Figure 5. Same as Fig. 4, but for other heavy rainfall events.

https://doi.org/10.5194/egusphere-2026-4109
Preprint. Discussion started: 4 August 2026

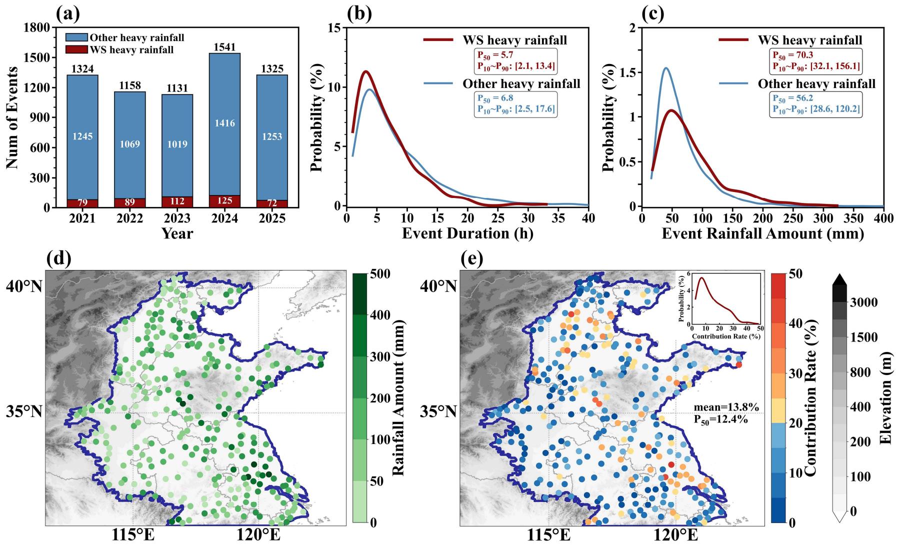

Figure 6. Comparison of WSHR and other heavy rainfall events during the warm seasons of 2021–2025. (a) Annual event counts (WS, dark red; other, light blue); numbers inside the bars are category counts, numbers atop are annual totals. (b) Probability density function (PDF) of event duration. (c) PDF of event cumulative rainfall amount. Legends in (b) and (c) give the median (P_{50}) and the 10th–90th percentile range (P_{10}–P_{90}). (d) Cumulative rainfall amount from WSHR events at each station in the study region. (e) Station-level contribution rate of WSHR to total heavy-rainfall accumulation; the inset shows the PDF of contribution rates across stations, with mean and P_{50} annotated.

https://doi.org/10.5194/egusphere-2026-4109
Preprint. Discussion started: 4 August 2026

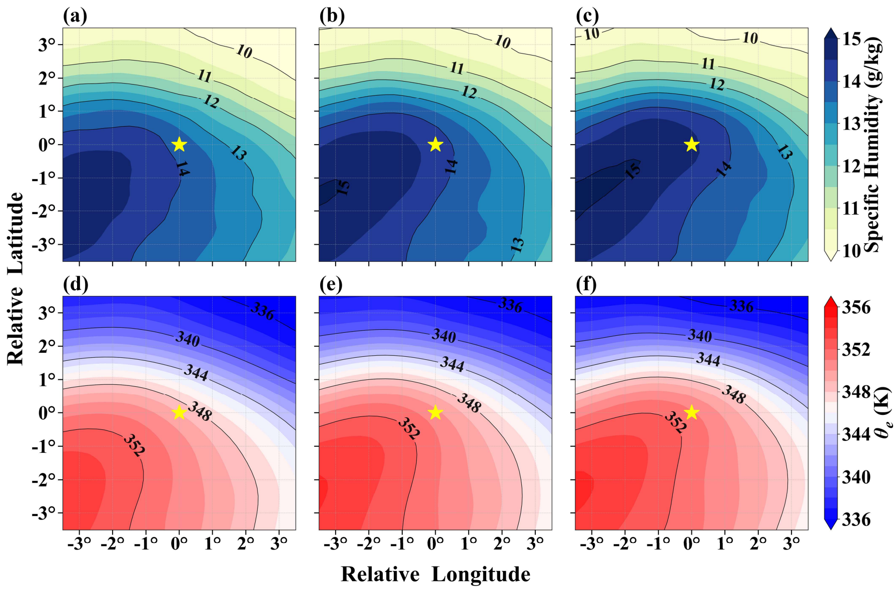

Figure 7. Composite 850-hPa specific humidity (a–c; shading, g kg^{-1}; contours every 1 g kg^{-1}) and pseudo-equivalent potential temperature θ_e (d–f; shading, K; contours every 4 K) fields for WSHR events, centered on the event target station (yellow star at origin). Columns correspond to 6 h before onset (a, d), 3 h before onset (b, e), and the onset hour (c, f).

https://doi.org/10.5194/egusphere-2026-4109
Preprint. Discussion started: 4 August 2026

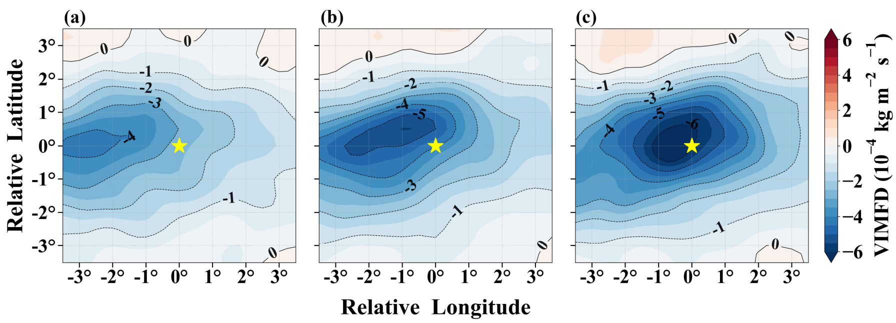

Figure 8. Composite low-level (1000–700 hPa) vertically integrated moisture flux divergence (VIMFD; shading, 10^{-4} kg m^{-2} s^{-1}; contours every 1×10^{-4} kg m^{-2} s^{-1}) for WSHR events, centered on the event target station (yellow star at origin). Panels correspond to 6 h before onset (a), 3 h before onset (b), and the onset hour (c). Negative values (blue) indicate moisture flux convergence.

https://doi.org/10.5194/egusphere-2026-4109
Preprint. Discussion started: 4 August 2026

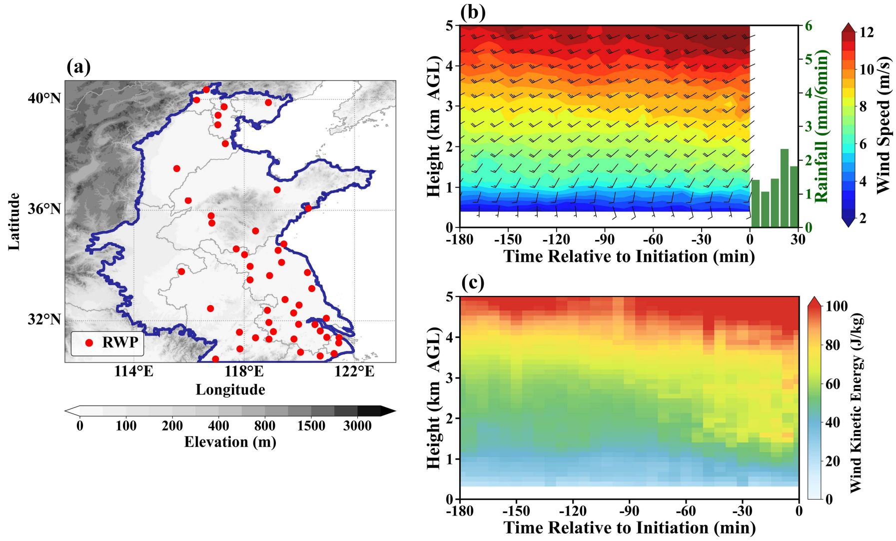

Figure 9. RWP observations and the composite time–height evolution of the low-level wind preceding the onset of WSHR events. (a) RWP stations with records of WSHR events (red dots) used to examine the precursor dynamic signals, overlaid on terrain elevation (grayscale, m). (b) Time–height composite of wind speed (shading, m s^{-1}) and wind barbs; green bars show composite rainfall (mm 6 min^{-1}, right axis). (c) Time–height composite of wind kinetic energy (shading, J kg^{-1}). In (b) and (c), the abscissa is time relative to the onset of rainfall (min) and the ordinate is height above ground level (km AGL).

https://doi.org/10.5194/egusphere-2026-4109
Preprint. Discussion started: 4 August 2026

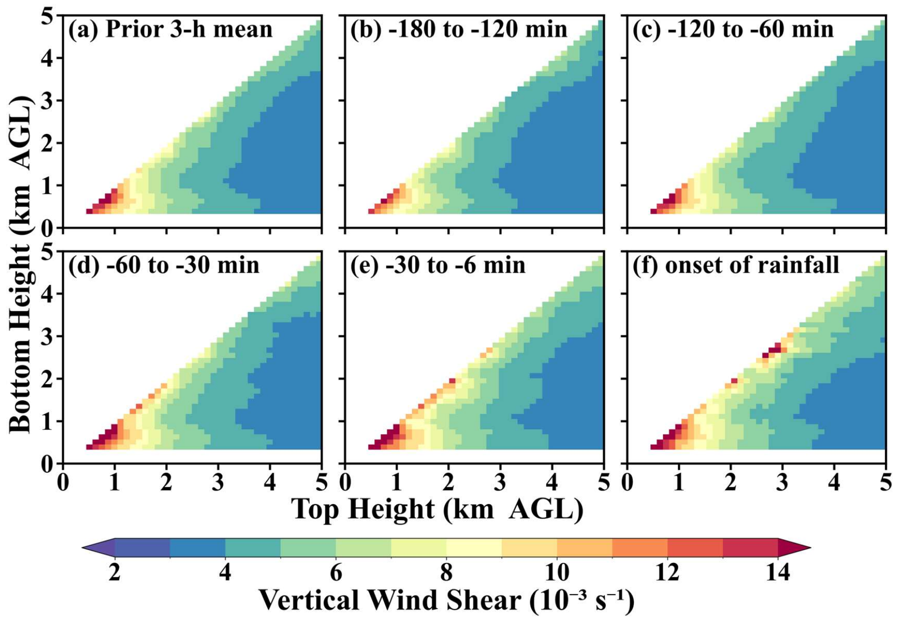

Figure 10. Composite vertical wind shear (shading, 10^{-3} s^{-1}) preceding the onset of WSHR events. (a) prior 3-h mean, (b) −180 to −120 min, (c) −120 to −60 min, (d) −60 to −30 min, (e) −30 to −6 min, and (f) the onset of rainfall. The abscissa and ordinate denote the top and bottom heights (km AGL), respectively, of the layer over which the bulk shear is computed.

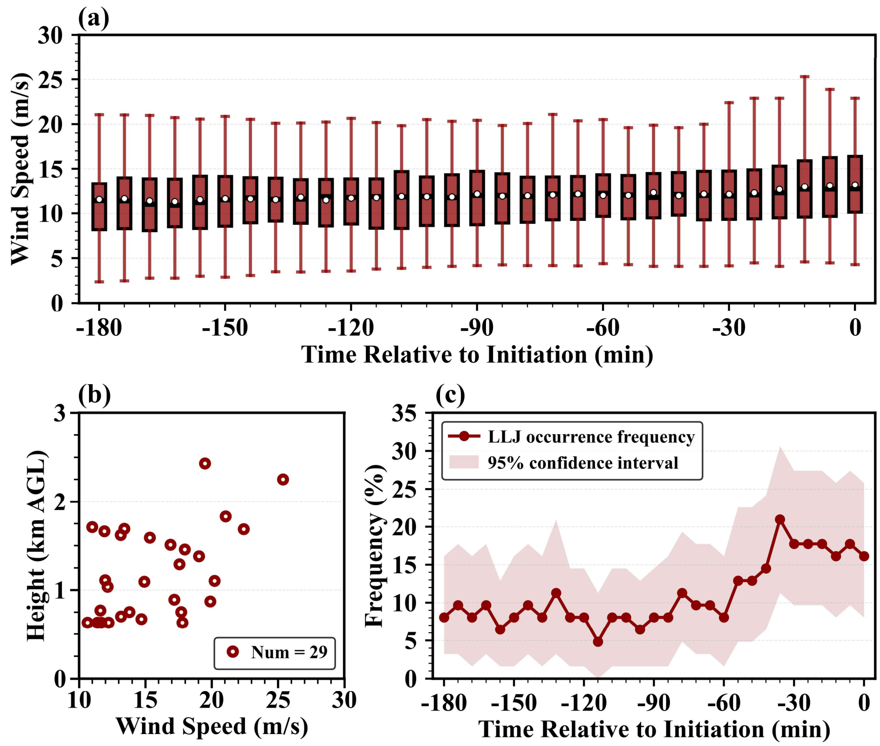

Figure 11. Low-level wind characteristics preceding the onset of WSHR events. (a) Box plots of the maximum wind speed below 3 km AGL within 180 min before the onset of WSHR events; for each box the central line denotes the median, the white circle with black edge denotes the mean, the box spans the interquartile range (25th–75th percentiles), and the whiskers extend to the 5th and 95th percentiles. (b) Mean core wind speed and mean core height of the low-level jet (LLJ), one marker per event containing an LLJ; Num is the number of such events. (c) Occurrence frequency of LLJs within 180 min before the onset of WSHR events. Shading in (c) denotes the 95% confidence interval derived from a bootstrap resampling of the 62 events (1000 iterations).

https://doi.org/10.5194/egusphere-2026-4109
Preprint. Discussion started: 4 August 2026

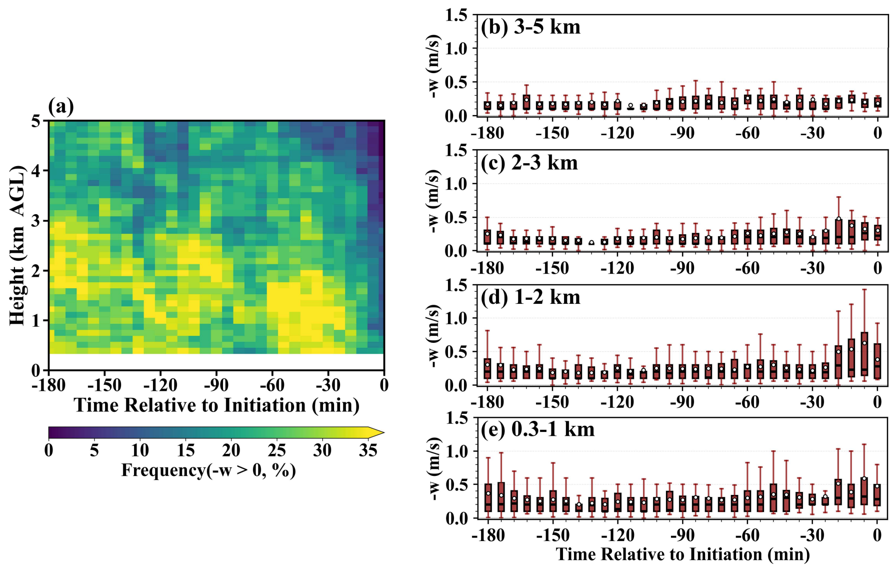

Figure 12. Composite ascending motion preceding the onset of WSHR events. (a) Frequency of ascending motion ($-w > 0$; %) as a function of height (km AGL) and time relative to the onset of WSHR events (min). (b–e) Box plots of the maximum ascent speed ($-w$; m s^{-1}) within 180 min before the onset of WSHR events at (b) 3–5 km, (c) 2–3 km, (d) 1–2 km, and (e) 0.3–1 km AGL.